Research Square

Preprints are preliminary reports that have not undergone peer review.
They should not be considered conclusive, used to inform clinical practice,
or referenced by the media as validated information.

Austenite Evolution during Incremental Cold Rolling of Ausformed and Tempered Ferrium M54

Joshua Edwards
Colorado School of Mines https://orcid.org/0000-0002-0110-7059
Adam Freund
Colorado School of Mines https://orcid.org/0009-0004-0795-8219
Ruben Ochoa
Colorado School of Mines https://orcid.org/0009-0006-6129-1317
Miranda Bell
Colorado School of Mines https://orcid.org/0000-0002-8259-7191
Suveen Mathaudhu
smathaudhu@mines.edu
Colorado School of Mines https://orcid.org/0000-0001-6248-5363

Research Article

Keywords: UHSS, rolling, austenite, martensite, texture

Posted Date: May 19th, 2026

DOI: https://doi.org/10.21203/rs.3.rs-9708780/v1

License: This work is licensed under a Creative Commons Attribution 4.0 International License.
Read Full License

Additional Declarations: The authors declare no competing interests.

Abstract

Ultrahigh strength steels (UHSS) have found utility in demanding engineering applications due to their excellent strength and toughness properties, which stem from microstructural features such as thin lath martensite, fine dispersed M_2C carbides, and a small fraction of retained austenite. The cold workability and corresponding microstructural evolution past the tempered state is not well understood. In this study, incremental (0.5–1% per pass) cold rolling of ausformed and tempered Ferrium M54 is characterized as a function of reduction levels using TEM phase and orientation mapping, and ASTAR-PED-derived texture analysis. Nanoscale phase mapping reveals a non-monotonic trend with austenite phase fraction generally increasing with rolling reductions near the surface from ~ 1.3% in the unrolled state to ~ 26.4% once 40% cold reduction is reached; decreasing to ~ 17.6% once cold rolling passes 40%. Textural analyses show an increase in textural sharpening up to the 40% cold rolled state, and then a decrease in sharping as the austenite phase fraction is reduced. The unique large-strain rolling conditions offer a framework under which the martensite to austenite phase transformation can occur at ambient temperatures. This work supports observations seen in theoretical models that observe similar non-monotonic phase transitions. These findings point to new opportunities to tailor martensite and austenite morphologies with goals of further improving mechanical performance in extreme environments.

1. Introduction

Ultrahigh strength steels (UHSS) are of interest to the transportation sector due to their high strength-to-weight ratios. Within this classification is the secondary-hardening class which utilizes high Co and Ni concentrations to for excellent strengthening and toughness combinations; alloys in this class include Aermet 100 [1], Ferrium S53 [2, 3], Ferrium M54 [4–6], M42 High Speed Steel [7], and others [8]. Fabrication of these alloys employs precise alloying (Co and Ni to reduce the martensite start temperature; strong carbide formers such as Mo, Cr, V, W) and a four-step thermomechanical schedule: 1) high-temperature (> 1000°C) annealing for homogeneous solid solution; 2) quenching to ambient; 3) cryocooling (~ − 75°C) to reduce retained austenite; 4) tempering to nucleate fine, dispersed M_2C (M = Mo, W, Cr, V) that pin dislocations. The resulting microstructure is tempered lath martensite containing fine dispersoids and controlled, but small (typically < 5 vol%) amounts of reverted austenite with island or film morphologies. These alloys reach ultimate tensile strengths > 2 GPa with tailored toughness via control of the reverted-austenite volume fraction, enabling their use in demanding environments.

Common to secondary hardening UHSS are tempered lath martensite hierarchies of packet–block–lath substructures that form during the post-annealing rapid quenching step [9, 10] following the Kurdjumov–Sachs (KS) orientation relationship [10–12]. At a much smaller length scale, nanoscale interlath retained austenite islands or films, typically 2–20 nm in width, have been documented at lath boundaries in the as-quenched conditions [13–15] with carbon diffusion and enrichment in these films contributing to their mechanical stability [16]. Control of the composition and content of austenite formers prior to tempering can allow for a controlled fraction of austenite to form during tempering, referred to as reverted or precipitated austenite [17]. Steels with such austenite films or islands in martensitic have demonstrated

excellent strength, ductility and toughness [18, 19]. While such superior properties are achievable in secondary hardening UHSS steels, review of the extant literature finds no reports on cold-working of these steels in the as-tempered state, nor the effects of microstructural evolution of the controlling phases (namely martensite and austenite), dislocation density, packet and lath sizes on the resulting properties.

Wider literature treats cold deformation of martensitic and martensite-containing steels almost exclusively as a step prior to a final tempering or partitioning treatment, where the cold-worked dislocation substructure either drives reverted austenite formation during a subsequent intercritical anneal - typically accompanied by a drop in yield strength [20, 21], or modulates secondary-phase precipitation during the aging step [22, 23]. Cold rolling applied after the final temper, particularly to a fully secondary-hardened UHSS in its peak-strength state, has not been systematically characterized. One barrier to extending cold rolling to a fully ausformed and tempered secondary-hardened UHSS is the hardness of the workpiece itself. For example, ausformed-and-tempered Ferrium M54 reaches a Vickers hardness of ~ 6.2 GPa (~ 630 HV/ ~57 HRC) in the bulk [24] and is worked using a two-high roll with roll hardness in the 61– 63 HRC range.

Cold-mill work rolls in conventional 4-high cold-rolling practice are forged, hardened alloy steels heat-treated to achieve a nominal hardness between ~ 62–67 HRC) [25, 26]. As such, the workpiece-to-roll hardness ratio approaches and, for the surface layers of cold-rolled material, exceeds unity. This regime violates the implicit assumption that the work rolls behave as quasi-rigid tools made of material substantially harder than the strip [25, 27, 28]: as workpiece flow stress approaches roll yield strength, contact-fatigue limits set in and reliable plastic deformation becomes infeasible without excessive tool wear.

One way to approach processing these secondary-hardened steels is with low-strain per pass rolling. While not a secondary hardening UHSS, Huang et al. have reported cold working of lath martensite ultralow carbon B- and Mn-containing interstitial free (IF) steel up to a reduction of 80% [29]. The reduction per rolling pass is unspecified, but the negligible hardening at low reductions and presence of sub-block boundaries (5% and 10%) implies low strains per pass. Increasing the strain to 30 and 50% resulted in a characteristic rolling structure in the martensite interconnected with cell boundaries and a decrease in the lamellar spacing with increased cold working. After 80% cold working, this spacing reduced to 200 nm, and the resultant material flow stress was 738 MPa. They summarized their work suggesting that the combination of martensitic structures, high dislocation densities and increased grain boundaries combined with certain elements in solid solution may result in high strength “nanometals” through plastic deformation, but without the requirements for ultrahigh strains.

While not explicitly reported, Huang et al. [29] likely used low strain rolling reductions to achieve such large strains. A separate body of industrial-process literature treats low-strain rolling of pre-finished steel sheet in the form of "skin-pass" or "temper" rolling. Conventionally, skin-pass rolling applies single-pass thickness reductions of 0.5–2% to annealed low-carbon steel strip to eliminate Lüders banding, set

surface texture, and control strain-aging behavior [30–33]. The contact mechanics of this regime have been characterized in detail and depart from those of conventional bulk-plastic rolling: at sub-2% per-pass reductions, an extended sticking region develops at the roll–strip interface, producing a wide, elasto-plastic deformation field rather than the continuously-yielding regime of high-reduction cold rolling [30–32, 34]. Recent work has extended this skin-pass regime to cumulative, multi-pass schedules in soft FCC metals: Yu et al. demonstrated that 40 cyclic skin-pass passes of ~ 1% per pass on annealed aluminum produces a gradient ultrafine-grained microstructure with a 206 nm surface mean grain size [35], establishing that cumulative low-per-pass schedules can lead to large structural refinement. Whether such an approach can be transferred to a BCC/BCT lath-martensite system, and to a fully tempered secondary-hardening UHSS, remains an open question.

The contact mechanics of skin-pass rolling suggest that it may be applicable to difficult to work materials, such as UHSS. At per-pass reductions below ~ 2%, the roll–strip contact develops an extended sticking region with strongly elasto-plastic, near-indentation character [31, 32, 36], rather than the continuously-yielding regime of conventional bulk-plastic rolling [27]. In this regime he rolling pressure and torque required for a given total reduction are a small fraction of those required to impose the same total reduction in a single pass [28, 34]; the contact geometry, rather than the workpiece flow stress, dominates the deformation kinematics. The same logic underpins multi-axial forging schedules used to accumulate large total strain in single-phase steels at room temperature, where small-strain-per-cycle, many-cycle deformation produces submicron-grained microstructures without the contact-pressure penalty of single-step large-strain processing [37, 38]. Although, the question remains on if similar cumulative phenomenon occurs in secondary hardened UHSS since skin-pass rolling has been demonstrated only in soft FCC metals[35].

Secondary-hardening Co–Ni UHSS alloys, with yield strengths exceeding 1.4 GPa and ultimate tensile strengths of $\sim$ 2 GPa, occupy a fundamentally different microstructural regime from conventional martensitic steels: a nearly fully martensitic matrix (98 % $+$) strengthened by coherent M $_2$C carbides. This leaves the question of whether low strain-per-pass approaches can drive substantive microstructural change in a BCC/BCT lath-martensite UHSS at workpiece-to-roll hardness ratios near unity. In Ferrium M54 specifically, the extended temper drives retained austenite to trace levels (< 1%); the austenite films observed in the as-tempered condition are instead reverted austenite, precipitated at lath boundaries during tempering [39, 40]. No study has examined the progressive microstructural evolution during multi-pass cold rolling of a tempered secondary-hardened UHSS, nor how the austenite films behave through the processing schedule. How the hierarchical lath architecture responds to cumulative reductions in these secondary hardened UHSS remains to be answered.

In this work, we demonstrate the successful skin pass rolling of ausformed and tempered Ferrium M54 to cold rolled (CR) reductions of ~ 60%, and characterize the microstructural evolution across the four CR conditions (0%, 20%, 40% and 60% cold work), documenting the hierarchical architecture, phase distribution, texture evolution, and intragranular strain state that underpin these mechanical

observations. Specific attention is given to the evolution of the total austenite morphology and volume fraction.

2. Materials and Methods

2.1 Samples Preparation

Ausformed and tempered Ferrium® M54® was provided in 4 mm thick plate form. The nominal composition shown in Table 1.

Table 1
Nominal composition of Ferrium M54 steel (wt. %, balance Fe).

Element	C	Co	Ni	Cr	Mo	W	V	Fe
wt. %	0.30	7.0	10.0	1.0	2.0	1.3	0.1	Bal.

The provided ausformed and tempered materials followed the schedule similar to that described by Sun et al. [24, 41], but were produced in an industrial mill. Samples were austenitized/solutionized at 1060 ◦C for 1 h in a box furnace. Following this step, the samples were furnace cooled for 30–60 min to achieve the ausforming temperature of 650 ◦C. Ausforming was accomplished through a nominal rolling reduction of 45% followed by fan cooling to room temperature, subzero cooling to -75 ◦C, and finally air warming back to ambient temperatures. The ausformed samples were then warm flattened and tempered at 515 ◦C for 9 h. The final step was another warm flattening and stress relief at 515 ◦C for 1h followed by air cooling. The resulting materials demonstrated nominal yield strength, hardness and percent elongation of 2.2 GPa, 630 HV (6.2 GPa) and 15% respectively, in alignment with Sun et al [24].

The ausformed and tempered plate was machined into a 3.8 mm-thick strip and subjected to cold rolling (CR) at ambient temperatures. Up to 65 rolling passes were performed with per-pass reductions of 0.5–1 %, yielding a cumulative thickness reduction of 61 % and a final thickness of 1.48 mm. The rolling speed was 0.05 m s^{-1} and the separating force peaked at 290 MPa ($\sim$ 42 ksi). Samples for microstructural characterization were sectioned perpendicular to the rolling direction (RD) and polished to reveal the normal direction–rolling direction (ND–RD) plane. Materials were examined in four approximate states of reduction: 0% (Unrolled), 20%, 40% and 60%.

2.2 ASTAR Precession Electron Diffraction and TEM

Transmission electron microscope (TEM) foils were prepared by focused ion beam (FIB) lift-out from specific locations on the cross-sectional (RD–ND) plane of each cold-rolled coupon. Automatic crystallography indexing and orientation/phase mapping (ASTAR) procession electron diffraction (PED) was performed on [42–44] cross-section liftouts using a 200 keV FEI Talos F200x S/TEM at ~ 150kx effective magnifications or greater.

ASTAR TopSpin procedures for beam alignment, precession correction, and phase identification were completed to obtain uniform-brightness diffraction spots across the observed scan area, typically 1–5 μ m FOV at 160 mm camera length. A precession angle of 0.5 $^\circ$ and a step size of 3 nm were used, and later processed with NanoMEGAS index 2 [45].

To extract an explicit morphological texture, the major-axis orientation of each ASTAR-reconstructed BCC grain was extracted by 2-D PCA on its boundary-smoothed pixel coordinates, area-weighted, and folded onto [− 90°, + 90°] (scan x-axis ∥ RD by construction). Template matching was performed for BCC ($\alpha\prime$ -martensite) and FCC (γ -austenite) phases with a confidence index threshold applied to exclude unreliably indexed pixels. Only grains with ≥ 20 pixels and aspect ratio ≥ 1.5 were retained, and border-touching grains were dropped. Three of the CR condition maps used over 100 grains for three CR conditions with the 40% CR condition resolving only 4 indexable grains and is reported for completeness only ASTAR-PED extrapolated GND density statistics by phase across the four CR conditions were calculated using a BCC median at 40 nm kernel-normalized scale, 90th-percentile and FCC median were calculated from the native-step distribution.

3 Results and Discussion

Using the small strain CR processing steps, skin pass rolling was achieved without excessive loads, no roll damage, and no cracking or fracture were observable in the samples, suggesting the applicability of this approach for materials beyond the easier to work FCC materials. Due to the small strain CR steps (0.5–1%), the plates deform more near the surface during the initial stages of rolling with deformation progressing towards the core/centerline as rolling strain increases. This results in a through-thickness “refinement front” that progresses from the rolled surface inward with increasing reduction.

3.1 Phase distribution and strain-induced austenite morphology

Phase distribution within 100 μ m from the rolled face is shown in Fig. 1 for the 0, 20%, 40% and 60% cold rolled conditions.

At 0% CR, reverted austenite is present as trace quantities (~ 1%) at lath boundaries and prior austenite grain boundaries, consistent with the interlath island or film morphology documented in as-quenched lath martensite systems [11, 13, 39]; the ASTAR-PED average boundary spacing in the cross-section core is 0.212 μm, establishing the A + T baseline for this study against which subsequent refinement is measured. The 20% CR maps show strong spatial heterogeneity in austenite distribution, with localized domains containing strain-induced austenite adjacent to near-zero-austenite regions, establishing that strain-induced austenite distribution is spatially heterogeneous from the earliest stages of cold work; the boundary spacing refines to 0.11 μm in the core.

At 40% CR, the austenite volume fraction has increased to 26.4 ± 9% at the surface and forms a connected, boundary-following interlath network with widths of 20–80 nm. The ASTAR-PED average boundary spacing in the cross-section core has refined to 0.077 ± 0.014 μm, while the surface value drops further to 0.037 μm — a surface/core gradient that will collapse by 60% CR. A characteristic feature of the 40% CR microstructure is the coexistence of large, uninterrupted martensite domains (remnant laths) with the surrounding fragmented, austenitic matrix. The remnant lath morphology is analogous to the large undeformed lath domains identified during early-stage plastic deformation of lath martensite [45–47].

At 60% CR, the strain-induced austenite "network" appears disrupted: austenite phase fraction reduces to 17.6% ± 8% and distributes uniformly throughout the cross-section with slight enrichment toward the core. Refined martensite laths reorganize into planar elongated features aligned with RD; the ASTAR-PED average boundary spacing in the cross-section core tightens from 0.077 ± 0.014 μm at 40% CR to 0.051 μm at 60% CR, and the surface value is comparable at 0.060 ± 0.020 μm, indicating that lath refinement is approximately homogeneous through-thickness at 60% CR — a contrast to the surface/core gradient evident at 40% CR (0.037 μm surface vs 0.077 μm core). These spacings correspond to lath thicknesses $\lesssim$ 30 nm under the elongated-lath aspect ratios visible in BF-STEM, comparable to the ~ 0.22 μm reported by Huang et al. [50] for lath martensite after 80% cold rolling, where the average boundary spacing, d_a is equal to ($2/S_v$) where S_v is the boundary area per unit volume, which aggregates the geometrically-necessary (GNB) and incidental-dislocation (IDB) boundary area per unit volume that subdivides the deformed lath structure into cell blocks [50].

Table 2 summarizes the quantitative phase fractions measured by ASTAR across all four CR conditions at surface and core (near centerline) positions. The observed trend of austenite-reversion between 40% and 60% CR is primarily observed near the rolled surface: austenite-fraction increases from 1.3 ± 1 % (0 % CR) to 26.4 ± 9 % (40 % CR surface), then decreases to 17.6 ± 8% (60 % CR). At the core, stain-induced austenite fractions remain below 15 % across all conditions.

Table 2
ASTAR-derived phase fractions (FCC γ-austenite; 0% represents reverted austenite, 20–60% refers to strain-induced austenite) by condition and cross-section position

CR %	Surface γ (%)	Core γ (%)	Trend
0 %	1.3 ± 0.9	2.6*	Trace; as-quenched baseline
20 %	0.5 ± 0.3	1.3*	Heterogeneous onset
40 %	26.4 ± 9	9.9*	Peak cellular network; ~3:1 surface:core
60 %	17.6 ± 8	12.6*	Partial retransformation
*Core microstructures are assumed to be homogenous along the ND-midplane, therefore median values presented for Core RA (%)			

Phase fraction results establish two defining characteristics of the austenite during incremental cold rolling. Firstly, it is non-monotonic, peaking at 40 % CR before partial retransformation to martensite at 60 % CR and secondly, it is depth-dependent, with the surface-to-core austenite ratio approaching 3:1 at 40 % CR. This through-thickness asymmetry motivates the grain-architecture analysis that follows.

The increase in austenite phase fractions at the higher rolling reductions bears discussion. Deformation typically drives the reversion of austenite to martensite, but under specific conditions, namely high shear stresses, the reverse transformation has been reported. Direct high-resolution TEM observation of the martensite to austenite (henceforth, BCC→FCC) reverse transformation in high pressure torsion (HPT) processed pearlitic steel (UIC 860) at room temperature was reported by MacLaren *et al.* [51]. The phase transformation preserved the KS orientation relationship across the boundary and was analyzed quantitatively by Ivanisenko *et al.* [52]. They postulated that the reverse martensitic transformation was stimulated by the high shear strains (~ 300) produced during HPT and severe microstructural refinement They present that an increase in the Gibbs free energy of ferrite due to the presence of nanocrystalline grains combined with the high-shear stresses produced during HPT supplies the driving force required for the reverse transformation. While the ambient temperature martensite-to-austenite transformation seen in the current study involves different phases, the rationale and framework presented by Ivanisenko holds true, and can be assumed to be at play at reductions greater than 40% CR.

3.2 Grain Architecture and Through-Thickness Refinement

Representative bright-field TEM and IPF maps for all four CR conditions are presented in Fig. 2; the corresponding ASTAR phase maps for the same surface regions are shown in Fig. 1. Across this strain series the lath skeleton evolves through three distinct stages: at 0% CR the packet–block hierarchy is well-resolved with prior austenite grains (PAGs) uniform throughout the cross-section; by 20% CR substructural heterogeneity is present at the surface but the core remains coarse and lath-dominant; at 40% CR a bimodal architecture has developed in which heavily fragmented, austenite-rich domains coexist with large, single-orientation “remnant lath” volumes; and by 60% CR these survivor domains are absent, the laths are pancaked, and the population converged to a unimodal, intermediate size.

The 40% CR condition is singled out for depth-resolved analysis because the phase-fraction asymmetry and bimodal grain-size distribution coincide there. The 40% CR microstructure demonstrates extensive, through thickness structural refinement, yet no sharp transitions were identified by microscopy alone. Near the rolling surface, the 40 % CR inverse pole figure (IPF) map shows extensive orientation fragmentation with sub-100 nm austenite domains. At the core, the lath packet–block hierarchy remains largely intact and resembles the 0 % CR baseline. The transition between these extremes is gradual rather than abrupt, with observations from the surface towards the core showing intermediate states of grain fragmentation. This gradient defines the spatial extent of what we term the “refinement front”; the boundary between heavily deformed surface and near-pristine core.

Bright-field TEM and ASTAR IPF maps across the CR series are captured in Fig. 2. Bright-field TEM tracks the lath morphology evolution; from clearly resolved individual laths at 0–40% CR (Fig. 2a-c) to tightly

packed, elongated features at 60% CR (Fig. 2d). Grain-boundary bulging is observed at an austenite pocket boundary in the 40% CR condition along the orange line parallel to the RD (Fig. 2b), consistent with localized deformation at austenite/martensite interfaces [16]. The disappearance of remnant-lath domains in the 60% CR (Fig. 2d), together with the transition from a heterogeneous phase distribution to uniformly dispersed residual austenite phase, marks the collapse of the bimodal architecture that characterizes the 40% CR state (Fig. 2c).At 40% CR, Fig. 2g reveals a large monolithic orientation domain, a remnant lath, with an orientation spread < 5°, consistent with a single crystallographic variant within the KS framework [12]. This domain is absent in the 60% CR map (Fig. 2h), where laths are strongly pancaked and homogeneously oriented along the RD. At 0 and 20% CR (Fig. 2e and Fig. 2f), the packet–block hierarchy from the as-quenched baseline is still recognizable, with substructural heterogeneity emerging only at the surface by 20% CR.

Grain-size distributions measured from ASTAR mapping are summarized in Table 3. The 40 % CR distribution is distinctly bimodal: a fine population (heavily fragmented austenite-rich zones peaking around 20–30 nm) coexists with a coarser population (remnant martensite laths between $\sim$ 250–350 nm). As such, the mean grain size of 37 nm at the surface is not fully representative of this distribution due to the bimodal nature. At 60 % CR, the distribution is unimodal and shifted toward intermediate grain sizes ($\sim$ 80–120 nm), concurrent with the loss of survivor-lath domains and the observed partial austenite reversion to martensite. The transition from bimodal to unimodal grain architecture between 40 and 60 % CR parallels the observed phase fraction reversal -(the condition of maximum austenite fraction corresponding to 40 % CR) and is coincident with the most heterogeneous grain size distribution.

Table 3
ASTAR-derived grain size statistics by condition and cross-section location. The bimodal character of the 40 % CR surface distribution is indicated by the simultaneous presence of a high %<50 nm fine population and a significant %>200 nm coarse population

CR	Loc.	Mean Grain Area	Median Grain Area	%< 50	%> 200	Characteristic
		(nm)	(nm)	nm	nm	
0 %	Surf.	62–75	60	35	5	Unimodal, lath mart.
0 %	Core	212	180	5	45	Coarser; PAGs uniform
20 %	Surf.	71–75	68	40	8	Heterogeneous onset
20%	Core	105	60–70	40–45	15–20	Coarse, largely still uniform PAGs
40 %	Surf.	37	—	60	20	Bimodal (fine+remnant)
40 %	Core	67–73	62	30	10	Bimodal; moderate refinement
60 %	Surf.	53–116	85	20	12	Unimodal; intermediate refinement
60 %	Core	51–57	50	40	5	Continued refinement

3.3 Texture Evolution and Fiber Analysis

Pole figures from ASTAR mapping (Fig. 3) reveal the evolution of crystallographic texture as a function of CR reduction. MUD values progress from $\sim$ 3–4 at 0 % CR, to $\sim$ 6–8 at 20 % CR, to 11.4 at 40 % CR, before decreasing to 5.1 at 60 % CR despite the increased rolling reduction. The progressive $\{001\}$//ND $\rightarrow$ $\{101\}$//RD rotation characteristic of BCC rolling textures [53] is confirmed at 20–40 % CR. In conventional BCC steels, α -fiber intensification is monotonic with increasing reduction, and MUD values rise continuously as grains accumulate $\langle 110\rangle$//RD orientations [54]. The M54 pole figures follow this expected progression through 40 % CR, where the $\{101\}$ projection (Fig. 3) shows progressive concentration of intensity along the RD, consistent with reported α -fiber behavior in BCC steels. However, the 60 % CR condition departs from the monotonic trend, and MUD decreases from 11.4 to 5.1 as the CR reduction increases from 60% to 80. A reversal not observed in conventional BCC rolling textures. This anomalous MUD decrease at 60 % CR coincides with the measured partial austenite phase reversion.

3.4 Lath Alignment and Morphological Texture

Pole figures and MUD are given in Fig. 4 and capture the crystallographic component of the rolling texture. The lath/packet morphology contributes a complementary, geometric component that the IPF maps in Fig. 2 suggest visually but do not quantify.

The 0% CR material has a pre-existing morphological texture with laths preferentially transverse to the imposed RD ($\langle\theta\rangle$ = +82°, r = 0.60), inherited from the cross-rolling step in the ausforming schedule; only ~ 3% of the area sits within ± 15° of RD. At 20% and 40% CR the lath population is in transition: the angular distribution broadens and the alignment strength drops to r = 0.36 and 0.28 respectively: laths are rotating through a near-isotropic regime *en route* to the rolling-aligned configuration. By 60% CR the laths have aligned strongly with RD ($\langle\theta\rangle$ = −3°, r = 0.93, 89% of area within ± 15° of RD and 97% within ± 30°), the canonical morphological signature of rolling-deformed lath martensite [14].

Alongside the pole-figure analysis (Fig. 3), this morphological texture supplies the missing geometric complement to the MUD trend. Crystallographic and morphological texture intensify together through 40% CR. The α-fiber MUD rising from 3.4 to 11.4 in parallel with the lath population beginning its rotation toward RD. At 60% CR the two textures decouple: the crystallographic MUD relaxes from 11.4 to 5.1 while the morphological alignment continues to sharpen to r = 0.93. This decoupling is consistent with two co-acting mechanisms: sub-block boundary sliding [51] permits packets to rotate as quasi-rigid units without further crystallographic re-orientation of the constituent variants, (allowing for martensitic laths to align geometrically without sharpening their shared crystal orientation) and strain-induced reversion of retained austenite [52] consumes the austenite islands and nucleates new BCC martensite variants whose orientations populate previously empty regions of the pole figure, dispersing the MUD even as the surviving lath skeleton converges on RD. Together, these mechanisms explain how M54 traverses the 60% CR reduction state with a partially relaxed crystallographic texture and a sharply RD-aligned morphological texture: a state in which strain has been accommodated by rotation and transformation rather than by classical work-hardening of the parent lattice.

3.5 Correlating microstructural refinement with γ-austenite evolution

The microstructural evolution across 0–60 % CR is not simply monotonic refinement. The phase distribution, grain architecture, crystallographic texture, grain sizes, and intragranular strain state are spatially and temporally correlated, producing distinct microstructural regimes at each reduction level.

In the as-quenched 0 % CR baseline, the microstructure is hierarchical but homogeneous: well-defined lath packets, trace reverted austenite at boundaries, near-random texture, and low stored strain energy. By 20 % CR, heterogeneity emerges: localized strain-induced austenite domains coexist with nearly austenite-free regions at the same depth, deformation features appear at lath boundaries, and texture begins sharpening. The heterogeneous character of this onset stage is a distinctive feature of the incremental CR process: the microstructural response to such CR is not spatially uniform from the earliest stages of deformation.

Table 4
ASTAR-PED extrapolated GND density statistics by phase across the four CR conditions

CR (%)	BCC median ρ (×10^{15} m^{-2})	BCC 90th-pct ρ (×10^{16} m^{-2})	FCC median ρ (×10^{16} m^{-2})	n grains (BCC)
0	1.6	4.8	6.5	34
20	6.3	4.2	3.3	46
40	7.9	5.7	3.8	4
60	6.3	5.0	3.2	24

By 40% CR, these correlated trends converge to a distinctive microstructural state. Peak strain-induced austenite fraction (26.4% ± 9% at the surface) coincides with maximum texture sharpness (MUD 11.4) and the emergence of a bimodal grain architecture (remnant laths + fragmented austenite-rich zones). This bimodal architecture is paralleled in the intragranular strain state: at fixed-step-size (40 nm) reporting, BCC GND median rises ~ 4× from 0% to 20% CR (1.6 → 6.3 × 10^{15} m^{-2}) and plateaus through 40–60% CR while the 90th-percentile remains pinned at ~ 5 × 10^{16} m^{-2} (Table 4), indicating that new dislocations populate lath interiors preferentially prior to affecting an already-saturated boundary network [29, 50]. The depth-resolved ASTAR sizing in Table 3 and the surface-to-core austenite asymmetry are shown to jointly indicate that this state is most pronounced at the surface and decays progressively toward the core, suggesting the presence of a "refinement front" that delineates the boundary between heavily transformed and near-intact microstructures.

Continued reduction to 60 % CR drives the refinement front deeper into the cross-section: the core mean grain size decreases from 67–73 nm at 40 % CR to 51–57 nm and the pronounced surface-to-core asymmetry in austenite fraction diminishes as both regions converge toward < 15 %. Despite this deeper penetration, the slight austenite-to-martensite reversion disrupts the phase architecture established at 40 % CR. The bimodal grain size distribution collapses to a unimodal intermediate population, concurrent with the disappearance of remnant-lath domains. Simultaneously, the texture randomizes (MUD decreasing from 11.4 to 5.1 despite increased rolling reduction), coincident with the partial reversion of austenite to fresh martensite. The net effect is a transition from the hierarchical, heterogeneous architecture of the 40 % CR state to a more homogeneous, uniformly refined microstructure, albeit one that retains 17.6 ± 8% austenite in elongated residual features.

The correlated progression of phase distribution, grain architecture, texture, and strain state across the four CR conditions indicates that these microstructural features do not evolve independently: increasing reduction produces a self-consistent combination of austenite fraction, grain morphology, texture sharpness, and intragranular strain. Three attributes of this evolution stand out. First, this architecture is reached at 60% nominal reduction (true strain $\varepsilon \approx 0.92$ past the ausformed and tempered state), comparable to the sub-100 nm grain populations reported in heavily cold-rolled lath martensite at 80–90% CR [28] but at substantially lower applied strain, because the rotation- and TRIP-mediated pathway absorb reduction without accumulating plastic shear in the parent lattice. Second, that same

combination (sub-block rotation, a sustained interlath austenite network, and ongoing TRIP-mediated reversion) maps onto the atomistic and crystallographic framework of Maresca and Curtin [53] in which the austenite/lath-martensite interface is glissile and athermal under resolved shear, so is expected to follow a Schmid-type law [56, 59]. The proposed pathway is asymmetric: the forward FCC→BCC branch is spontaneous while the reverse BCC→FCC branch requires high shear stresses (as asserted by Ivanisenko et al. [52] and paralleled in NiTi by Šittner *et al.* [59], who report distinct stress thresholds and plastic-strain magnitudes for the forward and reverse transformations under applied stress). Supplying a single mechanism for both deformation contributions of the interlath austenite network through 40% CR.

In conventional TRIP and dual-phase steels, cold rolling monotonically depletes reverted austenite via stress-assisted FCC→BCC transformation [55, 56]. The kinetics of this transformation follow the constitutive framework of Olson and Cohen [52, 55, 57], while the thermodynamic driving force is governed by the Patel–Cohen criterion [57, 58], which quantifies the mechanical work contribution to the transformation free energy. The Patel–Cohen mechanical work term — the dot product of the applied stress with the transformation shear — adds to the chemical driving force when the rolling stress component aligns with the transformation shape change.

When the mechanical term is positive for the reverse pathway (BCC→FCC) rolling stress can drive austenite formation even when the chemical ΔG favors martensite. This was clearly shown by Ivanisenko et al. [52] for HPT processed austenitic steels and is further validated by the findings herein for a nanostructured secondary hardening steel processed to large strains at ambient temperatures. M54's intermediate austenite stability (M_s reduced by Ni enrichment of residual films, in contrast to the bulk M_s of ≈ 200°C from the Carpenter datasheet [59]) combined with the high local shear stresses during incremental cold-rolling to large CR place it in precisely the regime needed for the reverse martensite to austenite to occur [52, 58]. The 90th-percentile GND saturation reported in Table 4 is consistent with a parent lattice still below the dislocation density at which interface mobility would be impaired.

Lastly, the contribution of austenite to toughness in lath martensite depends on its type, distribution, and morphology rather than on volume fraction alone: elongated interlath films and blocky prior-austenite islands deform and revert differently under strain [13, 16, 49]. Whether the interlath-film architecture documented here yields the strength–toughness response this mechanism predicts, and how the CR schedule controls the balance between film and blocky morphologies during reduction, are open questions that direct mechanical testing of CR-conditioned M54 will be required to resolve.

4. Conclusion

Ausformed and tempered Ferrium M54 was successfully cold rolled with small strain reduction passes to a reduction of 60% with no large-scale flaws, cracks or resultant fracture. The ensuing microstructural evolution was characterized across four cold-rolling conditions (0, 20, 40, 60 % CR), and reveals the following:

1. Skin-pass rolling, or other incremental deformation approaches may be suitable for cold processing of difficult-to-work materials including emerging high strength steel alloys and high stacking fault materials.
2. Cold rolling-induced austenite forms as an interconnected interlath network at lath boundaries (20–80 nm feature widths, 26.4 ± 9 % volume fraction at the 40 % CR rolling surface), morphologically distinct from the blocky prior austenite grain boundary austenite of as-quenched UHSS alloys. The strain induced reverse transformation of martensite to austenite is consistent with severe plastic deformation studies that have observed similar phase transformations due to large shear stresses and an increase of Gibbs free energy in the starting phase due to non-equilibrium nanostructured domains.
3. Incremental CR results in a bimodal microstructure: at 40 % CR, laths that were partially resistant to fragmentation based on crystallographic orientation effects “remnant laths” (large, coherent single-orientation domains) coexist with heavily fragmented austenite-rich zones.
4. As CR increases, crystallographic texture sharpens progressively from MUD $\sim$ 3–4 at 0 % CR to 11.4 at 40 % CR via $\{001\}$//ND $\rightarrow$ $\{101\}$//RD rotation, then decreases anomalously to 5.1 at 60 % CR coincident with minor reversion.
5. Lath morphological texture evolves non-monotonically: a pre-existing transverse cross-rolled state (r = 0.60 at 0% CR) passes through a near-isotropic transitional regime at 20–40% CR (r = 0.36, 0.28) before converging to a strongly RD-aligned configuration at 60% CR ($\langle\theta\rangle \approx -3°$, r = 0.93, 89% of grain area within ± 15° of RD), supplying the geometric complement to the crystallographic texture trend.
6. Depth-resolved ASTAR grain sizing at 40 % CR (Table 3), together with the surface-to-core austenite asymmetry, documents a hierarchical depth gradient from a heavily refined, austenite-rich surface to near-intact lath martensite at the core.

Observed interlath austenite morphology is consistent with prior observations of austenite films in lath martensite systems [13, 16], though the CR-induced network architecture documented here, with feature widths of 20–80 nm and local fractions exceeding 26.4 ± 9 %, has not previously been reported in a secondary-hardening UHSS. These finding suggest further tailorability of the already excellent annealed/homogenized/ausformed and tempered properties in UHSS steels through further cold-working to decrease lath size, increase dislocation density and control the volume fraction of austenite that lends the alloys enhanced toughness. The role of these microstructural features on hardness and the mechanical properties will be examined in a future study.

Declarations

Declaration of generative AI and AI-assisted technologies in the manuscript preparation process

No generative AI tools or AI-assisted technologies were used during the preparation of this work. The authors reviewed and edited the content as needed and take full responsibility for the content of the published article.

CRediT Author Contribution Statement

Joshua Edwards: Conceptualization, Methodology, Investigation, Writing – Original Draft, Visualization. Adam Freund: Investigation, Formal analysis. Ruben Ochoa: Investigation. Miranda Bell: Writing – Review & Editing. Suveen Mathaudhu: Conceptualization, Supervision, Writing – Review & Editing, Project administration, Funding acquisition.

Acknowledgments

Joshua Edwards and Suveen Mathaudhu acknowledge support and materials from QuesTek Innovations LLC. Joshua Edwards was supported via the Department of Education, Graduate Assistance in Areas of National Need (GAANN) Fellowship, under grant #P200A210134. The Tescan S8252G was acquired through the support of the National Science Foundation (DMR-1828454).

Data Availability

Data will be made available upon request

References

1. Analysis T, Information G, Resistance C (1994) Aermet 100 Alloy. Alloy Digest 43:1–10. https://doi.org/10.31399/asm.ad.fe0107
2. Carpenter, Technology (2025) Ferrium_S53_Datasheet
3. Charles J, Kuehmann GB, Olson H-J, Jou (2011) NANOCARBIDE PRECIPITATION STRENGTHENED ULTRAHIGH-STRENGTH, CORROSION RESISTANT, STRUCTURAL STEELS, US7967927B2
4. Lee EU, Stanley M, Pregger B, Lei C, Lipnickas E (2015) Ferrium M54 steel. Naval Air Warfare Center Aircraft Div Patuxent River MD
5. QuestTek I, Llc Ferrium® M54® steel datasheet, 2015.
6. Jou HJ (2015) Lower-cost, ultra-high-strength, high-toughness steel. US 9(051):635 B2
7. Carpenter, Technology (1991) CarTech M42 High Speed Steel Datasheet
8. Yang C, Li Y, Han S, Pang X, Geng R, Li X, Wang C (2025) Effects of Solid–Solution Temperature on Microstructures and Mechanical Properties of 2200 MPa Grade Secondary Hardening Steel. Materials 18:2126. https://doi.org/10.3390/ma18092126
9. Bhadeshia HKDH, Honeycombe R (2006) Modeling of microstructure and properties, in: Steels: Microstructure and Properties, 3rd ed., Butterworth-Heinemann, : p. 318. https://doi.org/10/fmbdwb
10. Krauss G (1999) Martensite in steel: Strength and structure. Mater Sci Eng A 273–275. 40–57. https://doi.org/10.1016/s0921-5093(99)00288-9

11. Morito S, Huang X, Furuhara T, Maki T, Hansen N (2006) The morphology and crystallography of lath martensite in alloy steels. Acta Mater 54:5323–5331. https://doi.org/10.1016/j.actamat.2006.07.009
12. Kitahara H, Ueji R, Tsuji N, Minamino Y (2006) Crystallographic features of lath martensite in low-carbon steel. Acta Mater 54:1279–1288. https://doi.org/10.1016/j.actamat.2005.11.001
13. Morsdorf L, Jeannin O, Barbier D, Mitsuhara M, Raabe D, Tasan CC (2016) Multiple mechanisms of lath martensite plasticity. Acta Mater 121:202–214. https://doi.org/10.1016/j.actamat.2016.09.006
14. Morito S, Tanaka H, Konishi R, Furuhara T, Maki T (2003) The morphology and crystallography of lath martensite in Fe-C alloys. Acta Mater 51:1789–1799. https://doi.org/10.1016/S1359-6454(02)00577-3
15. Jung J, Jun J-H, Lee Y-K (2014) The microstructure of lath martensite in quenched 9Ni steel. Acta Mater 68:168–178. https://doi.org/10.1016/j.actamat.2014.01.007
16. Morsdorf L, Tasan CC, Ponge D, Raabe D (2015) Carbon enrichment in retained austenite films and the influence on mechanical stability. Acta Mater 95:366–377. https://doi.org/10.1016/j.actamat.2015.05.023
17. Mondiere A, Déneux V, Binot N, Delagnes D (2025) Control of retained austenite stability during the heat treatment of the high performance steel ferrium® M54®. J Mater Res Technol 36:2074–2082. https://doi.org/10.1016/j.jmrt.2025.03.230
18. Li Y, Yuan G, Li L, Kang J, Yan F, Du P, Raabe D, Wang G (2023) Ductile 2-GPa steels with hierarchical substructure. Science 379:168–173. https://doi.org/10.1126/science.add7857
19. Shan B, Zhang H, Mi P, Li X, Liu Z, Guo Y, Xu B, Sun M (2025) Tracing the evolution of hierarchical microstructures and its effect on the mechanical properties of a secondary hardening ultra-high strength steel. J Mater Res Technol 39:4983–4995. https://doi.org/10.1016/j.jmrt.2025.10.184
20. Hosseinifar F, Ekrami A (2022) The effect of cold-rolling prior to the inter-critical heat treatment on microstructure and mechanical properties of 4340 steel with ferrite – martensite microstructure. Mater Sci Eng A 830:142314. https://doi.org/10.1016/j.msea.2021.142314
21. Niu G, Tang Q, Zurob HS, Wu H, Xu L, Gong N (2019) Strong and ductile steel via high dislocation density and heterogeneous nano/ultrafine grains. Mater Sci Eng A 759:1–10. https://doi.org/10.1016/j.msea.2019.04.112
22. Padhy GK, Others (2024) Effect of prior cold rolling and aging temperature on PH martensitic stainless steel: evolution of microstructure, micro-texture and austenite stability. Mater Charact 208:113600. https://doi.org/10.1016/j.matchar.2024.113600
23. Huang JX, Liu Y, Xu T, Chen XF, Lai QQ, Xiao LR, Pan ZY, Gao B, Zhou H, Zhu YT (2022) Dual-phase hetero-structured strategy to improve ductility of a low carbon martensitic steel. Mater Sci Eng A 834. https://doi.org/10.1016/j.msea.2021.142584
24. Sun Y, Quan J, Salvador H, Edwards J, Lin J, Kozmel T, Mathaudhu S (2022) Ausforming and tempering of a novel ultra-high strength steel. Mater Sci Eng A 838:142750. https://doi.org/10.1016/j.msea.2022.142750

25. Roberts WL (1978) Cold rolling of steel. M. Dekker, New York
26. Krauss G (2015) Steels: processing, structure, and performance, 2nd edn. ASM International, Materials Park, Ohio
27. Sims RB (1954) The Calculation of Roll Force and Torque in Hot Rolling Mills, Proceedings of the Institution of Mechanical Engineers 168 191–200. https://doi.org/10.1243/PIME_PROC_1954_168_023_02
28. Lenard JG (2002) Metal Forming Science and Practice: A State-of-the-Art Volume in Honour of Professor J.A. Schey's 80th Birthday
29. Huang X, Morito S, Hansen N, Maki T (2012) Ultrafine structure and high strength in cold-rolled martensite. Metall Mater Trans A 43:3517–3531. https://doi.org/10.1007/s11661-012-1275-5
30. Kijima H, Bay N (2008) Skin-pass rolling II-Studies of roughness transfer under combined normal and tangential loading. Int J Mach Tools Manuf 48:1308–1312. https://doi.org/10.1016/j.ijmachtools.2008.06.006
31. Kijima H, Bay N (2007) Contact conditions in skin-pass rolling, CIRP Annals - Manufacturing Technology 56. 301–306. https://doi.org/10.1016/j.cirp.2007.05.070
32. Kijima H, Bay N (2008) Skin-pass rolling I-Studies on roughness transfer and elongation under pure normal loading. Int J Mach Tools Manuf 48:1313–1317. https://doi.org/10.1016/j.ijmachtools.2008.06.005
33. Schneeweis R, Berger K, Mathweis D (2020) Advancement of skin pass rolling, Tecnol. Em Metal Mater Min 17:131–136. https://doi.org/10.4322/2176-1523.20202222
34. Yuen WYD, Dixon A, Nguyen DN (1996) The modelling of the mechanics of deformation in flat rolling. J Mater Process Technol 60:87–94. https://doi.org/10.1016/0924-0136(96)02312-6
35. Yu H, Lu C, Tieu K, Li H, Godbole A, Liu X, Kong C (2019) Microstructure and mechanical properties of large-volume gradient-structure aluminium sheets fabricated by cyclic skin-pass rolling. Philos Mag 99:2265–2284. https://doi.org/10.1080/14786435.2019.1619948
36. Giarola AM, Pereira PHR, Stemler PA, Pertence AEM, Campos HB, Aguilar MTP, Cetlin PR (2015) Strain heterogeneities in the rolling direction of steel sheets submitted to the skin pass: A finite element analysis. J Mater Process Technol 216:234–247. https://doi.org/10.1016/j.jmatprotec.2014.09.015
37. Belyakov A, Kimura Y, Tsuzaki K (2005) Recovery and recrystallization in ferritic stainless steel after large strain deformation. Mater Sci Eng A 403:249–259. https://doi.org/10.1016/j.msea.2005.05.057
38. Belyakov A, Tsuzaki K, Kimura Y (2008) Regularities of deformation microstructures in ferritic stainless steels during large strain cold working. ISIJ Int 48:1071–1079. https://doi.org/10.2355/isijinternational.48.1071
39. Zhu H, Xiong Z, Mao J, Cheng X (2025) Achieving ultra-high strength, good toughness and cost reduction in secondary hardening steel via dual precipitation. Mater Charact 223:114869. https://doi.org/10.1016/j.matchar.2025.114869

40. Zhu H, Xiong Z, Mao J, Cheng X (2025) Effect of solid-solution temperature on the microstructure and mechanical properties in low-cobalt secondary hardening ultra-high strength steel. Procedia Struct Integr 69:113–120. https://doi.org/10.1016/j.prostr.2025.07.016
41. Mondiere A, Déneux V, Binot N, Delagnes D (2018) Controlling the MC and M2C carbide precipitation in ferrium® M54® steel to achieve optimum ultimate tensile strength/fracture toughness balance. Mater Charact 140:103–112. https://doi.org/10.1016/j.matchar.2018.03.041
42. Rauch EF, Véron M (2014) Automated crystal orientation and phase mapping in TEM. Mater Charact 98:1–9. https://doi.org/10.1016/j.matchar.2014.08.010
43. Rauch EF, Portillo J, Nicolopoulos S, Bultreys D, Rouvimov S, Moeck P (2010) Orientation and phase mapping in the transmission electron microscope using precession-assisted diffraction spot recognition: state-of-the-art results. Z Krist 225:103–109. https://doi.org/10.1524/zkri.2010.1205
44. Rauch EF, Véron M (2021) New features in crystal orientation and phase mapping for transmission electron microscopy. Symmetry 13:1675. https://doi.org/10.3390/sym13091675
45. Smith H, Linke BS, Muránsky O, Hamelin C, Hill MR (2020) Assessment of mechanical properties and microstructure characterizing techniques in their ability to quantify amount of cold work in 316L alloy. J Eng Mater Technol 142:041005. https://doi.org/10.1115/1.4047024
46. Mondiere A, Déneux V, Binot N, Delagnes D (2018) Controlling the MC and M2C carbide precipitation in Ferrium® M54® steel to achieve optimum ultimate tensile strength/fracture toughness balance. Mater Charact 140:103–112. https://doi.org/10.1016/j.matchar.2018.03.041
47. Michiuchi M, Nambu S, Ishimoto Y, Inoue J, Koseki T (2009) Relationship between local deformation behavior and crystallographic features of as-quenched lath martensite during uniaxial tensile deformation. Acta Mater 57:5283–5291. https://doi.org/10.1016/j.actamat.2009.07.026
48. Du C, Hoefnagels JPM, Vaes R, Geers MGD (2016) Plasticity of lath martensite by sliding of substructure boundaries. Scripta Mater 120:37–40. https://doi.org/10.1016/j.scriptamat.2016.04.006
49. Raabe D, Sandlöbes S, Millán J, Ponge D, Assadian H, Herbig M, Choi P-P (2013) Segregation engineering enables nanoscale martensite to austenite phase transformation at grain boundaries: a pathway to ductile martensite. Acta Mater 61:6132–6152. https://doi.org/10.1016/j.actamat.2013.06.055
50. Huang X, Morito S, Hansen N, Maki T (2012) Ultrafine structure and high strength in cold-rolled martensite. Metall Mater Trans A 43:3517–3531. https://doi.org/10.1007/s11661-012-1275-5
51. MacLaren I, Ivanisenko Y, Valiev RZ, Fecht HJ (2006) Reverse martensitic transformation of ferrite to austenite under severe plastic deformation. J Phys Conf Ser 26:335–338. https://doi.org/10.1088/1742-6596/26/1/081
52. Ivanisenko Y, Maclaren I, Sauvage X, Valiev R, Fecht H (2006) Shear-induced α→γ transformation in nanoscale Fe–C composite. Acta Mater 54:1659–1669. https://doi.org/10.1016/j.actamat.2005.11.034

53. Raabe D, Lucke K (1994) Rolling textures in steels. Scr Metall Mater 27:1533–1538. https://doi.org/10.1016/0956-716X(92)90085-E
54. Hölscher M, Raabe D, Lücke K (1991) Rolling and recrystallization textures of bcc steels. Steel Res 62:567–575. https://doi.org/10.1002/srin.199100451
55. Huang X, Morito S, Hansen N, Maki T (2012) Ultrafine structure and high strength in cold-rolled martensite. Metall Mater Trans A 43:3517–3531. https://doi.org/10.1007/s11661-012-1275-5
56. Maresca F, Kouznetsova VG, Geers MGD (2014) On the role of interlath retained austenite in the deformation of lath martensite. Modell Simul Mater Sci Eng 22:045011. https://doi.org/10.1088/0965-0393/22/4/045011
57. Olson GB, Cohen M (1975) Kinetics of strain-induced martensitic nucleation. Metall Trans A 6:791–795. https://doi.org/10.1007/bf02672301
58. Maresca F, Kouznetsova VG, Geers MGD, Curtin WA (2018) Contribution of austenite-martensite transformation to deformability of advanced high strength steels: From atomistic mechanisms to microstructural response. Acta Mater 156:463–478. https://doi.org/10.1016/j.actamat.2018.06.028
59. Šittner P, Heller L, Iaparova E, Kadeřávek L, Molnárová O, Tyc O (2025) Generation of plastic strains by the martensitic transformations under stress via dislocation slip in martensite as the origin of functional fatigue, Shape Mem. Superelasticity 11:679–707. https://doi.org/10.1007/s40830-025-00550-z
60. Olson GB, Cohen M (1982) Stress-assisted isothermal martensitic transformation: application to TRIP steels. Metall Trans A 13:1907–1914. https://doi.org/10.1007/BF02645934
61. Fisher JC, Hollomon JH, Turnbull D (1949) Kinetics of the austenite→martensite transformation, JOM 1. 691–700. https://doi.org/10.1007/BF03398922
62. Zecevic M, Upadhyay MV, Polatidis E, Panzner T, Van Swygenhoven H, Knezevic M (2019) A crystallographic extension to the olson-cohen model for predicting strain path dependence of martensitic transformation. Acta Mater 166:386–401. https://doi.org/10.1016/j.actamat.2018.12.060
63. Patel JR, Cohen M (1953) Influence of stress on the martensite transformation. Acta Metall 1:531–538. https://doi.org/10.1016/0001-6160(53)90083-2
64. Carpenter Technologies (2025) Corporation, Ferrium M54 Datasheet

Figures

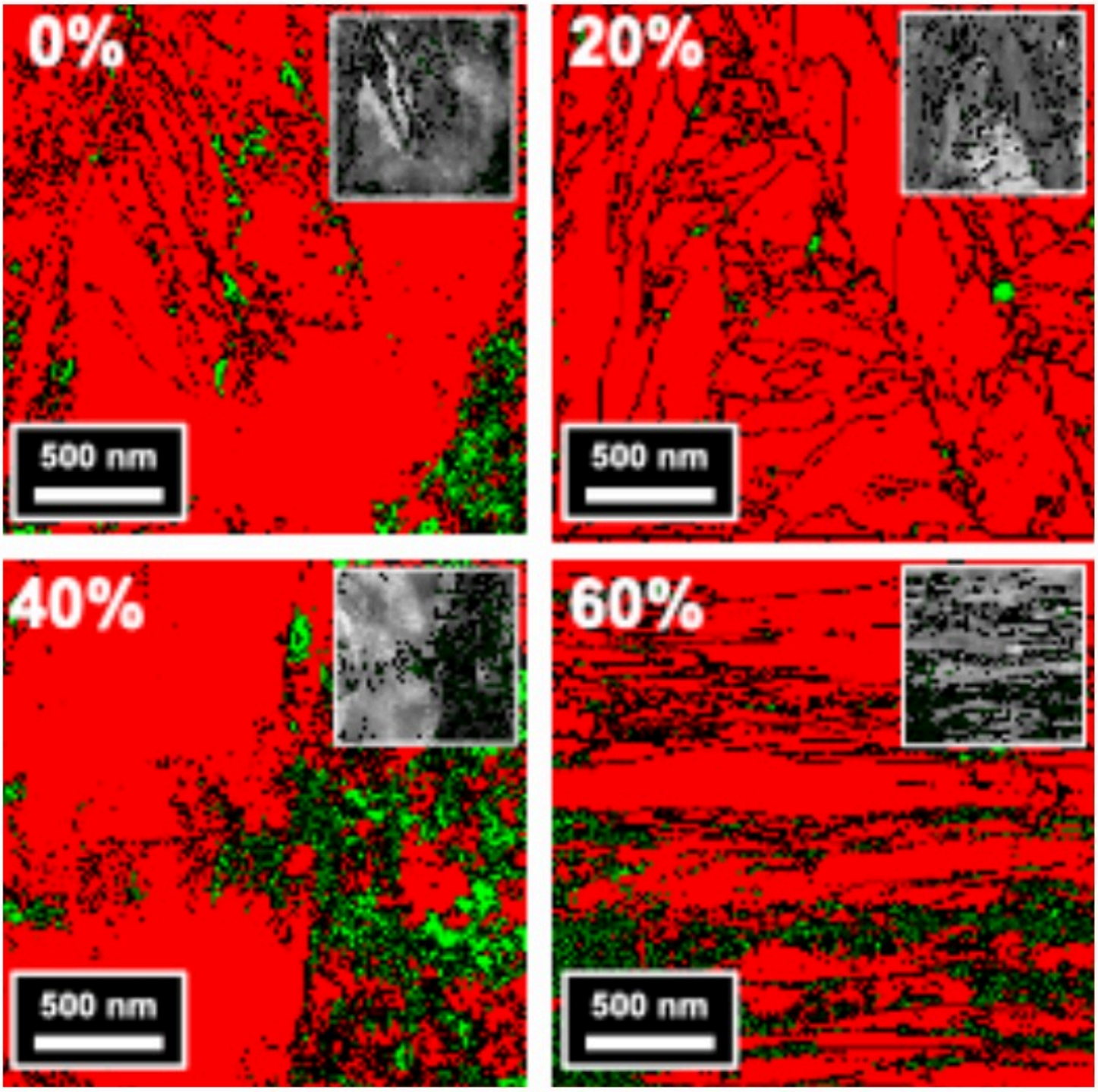


Figure 1

Representative ASTAR phase maps with TEM bright-field insets at the surface for all four cold-rolling conditions. The BCC α'-martensite is shown red and FCC γ-austenite is shown in green. Unindexed pixels (high dislocation density regions) are shown in black. The typical microstructure transitions from trace boundary reverted austenite (0% CR) to rough cellular networks (40% CR) to elongated residual films (60% CR).

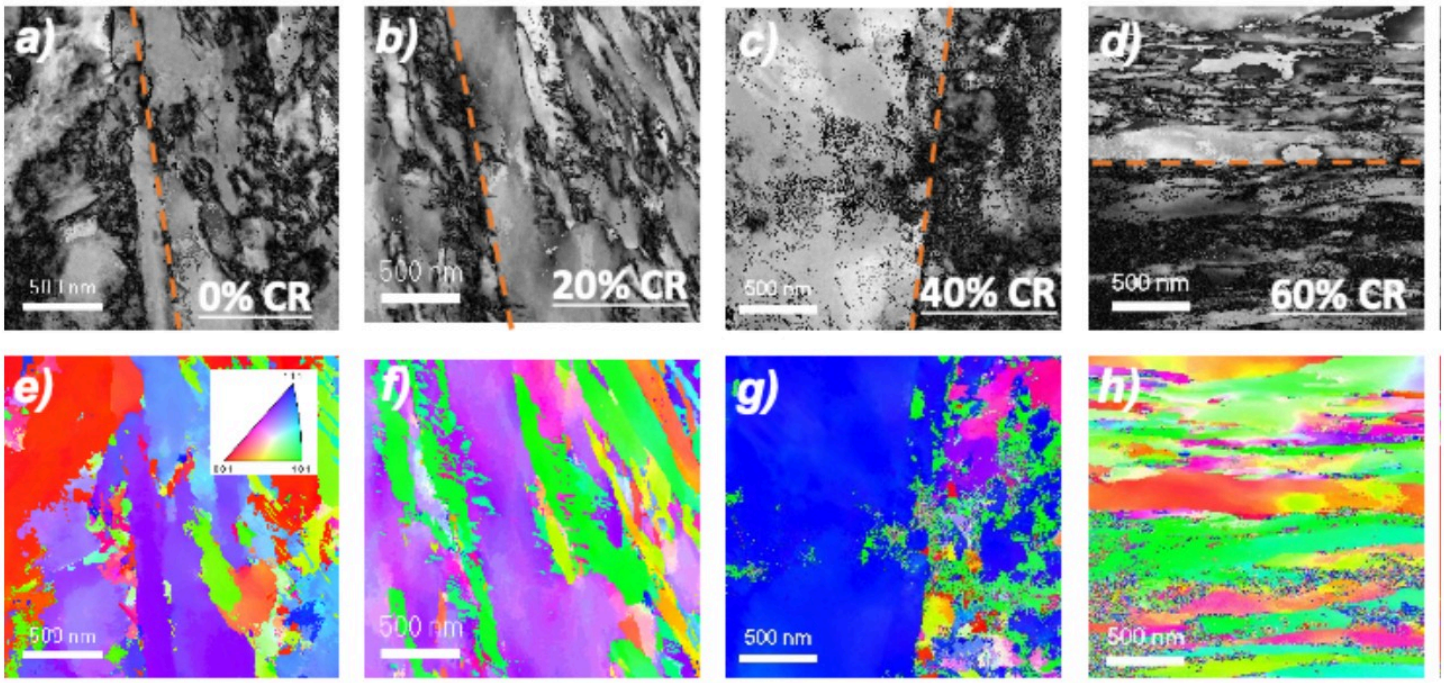


Figure 2

Representative microstructural progression across cold-rolling reductions: 0 % CR (a, e), 20 % CR (b, f), 40 % CR (c, g), and 60 % CR (d, h). (a–d) Bright-field TEM showing lath morphology evolution; orange line in (c) marks the major-axis direction of a prior-austenite boundary in the 40 % CR condition. (e–h) IPF maps (RD ‖ x-axis) showing orientation distribution; the large monolithic orientation domain ("remnant lath") visible in (g) is absent in (h). IPF color key inset in (e). Corresponding ASTAR phase maps for the same surface regions appear in Fig. 1.

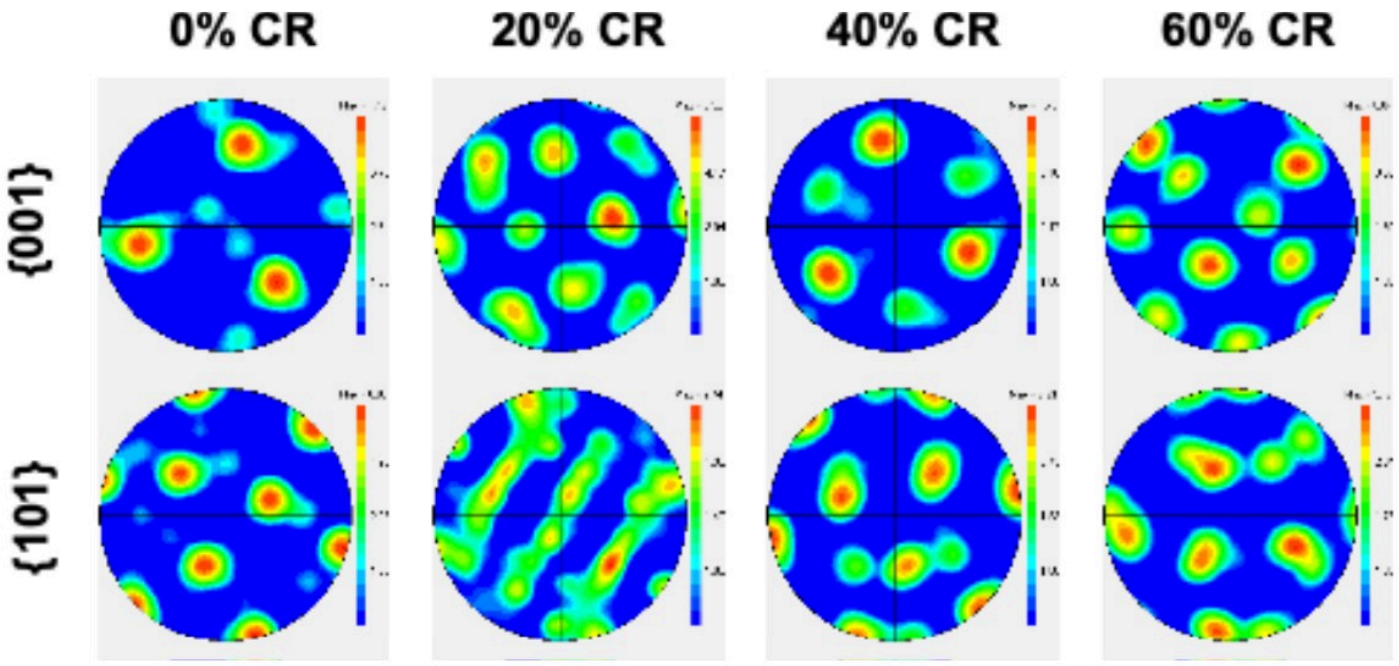


Figure 3

{001} (top row) and {101} (bottom row) pole figures for the four cold-rolling conditions (surface region), calculated from ASTAR-PED data; MUD values annotated per condition. The {101} projection captures the BCC α-fiber (⟨110⟩ ∥RD) signature, intensifying through 40 % CR; the {001} projection [52] resolves the cube subspace (cube, rotated cube, {001}⟨110⟩), with intensity migrating off ND toward rotated-cube and α_1 positions as reduction proceeds. Both signatures broaden at 60 % CR coincident with austenite reversion. The {101} pole figure (Fig. 3) tracks the BCC α-fiber (⟨110⟩ ∥RD) as intensity concentrating along RD; the {001} pole figure tracks the cube subspace ({001}⟨110⟩ rotated cube and {112}⟨110⟩) as intensity migrating off the ND center. γ-fiber components ({111} ∥ND) are not separately resolved by this {001}+{101} pair. At 0 % CR the texture is near-random (MUD ∼3–4) with no dominant fiber, consistent with the prior-austenite grain structure inherited through the K–S relationship. Progressive cold rolling preferentially strengthens the α-fiber: the {001}⟨110⟩and {112}⟨110⟩ components intensify through 40 % CR, tracking the canonical {001} ∥ ND → {101} ∥ RD rotation reported for BCC rolling textures [49]. Texture sharpening through this regime is generally accompanied by increasing dislocation density and substructure refinement [48,50]. The crystallographic texture captured in Fig. 3 is one component of the rolling-deformation signature; the morphological alignment of the lath/packet hierarchy is discussed next.

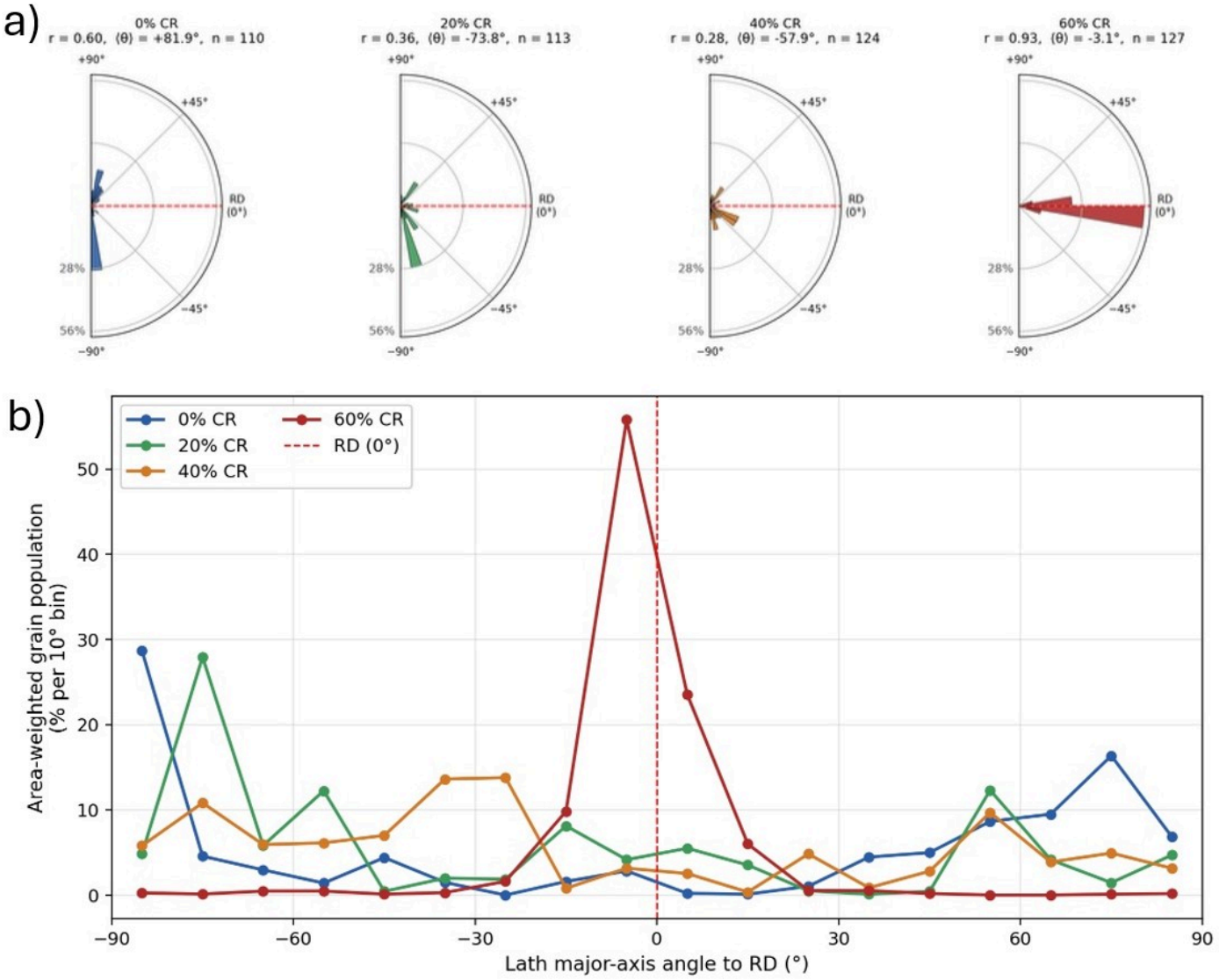


Figure 4

Martensite lath/packet major-axis alignment to RD across the four CR conditions. **(a)** Half-rose diagrams (axially folded angular distributions, area-weighted by grain pixel count, minimum 100 lath per CR condition). **(b)** Linear overlay histogram with per-condition summary table inset (⟨θ⟩: Median angle to RD major axis, r: axial alignment strength (0 = isotropic, 1= all parallel), n: number of indexed laths). 0 % CR exhibits a transverse cross-rolled texture (⟨θ⟩ = +82°, r = 0.60); 20–40 % CR are transitional (r = 0.36, 0.28); 60 % CR converges to RD-aligned (⟨θ⟩ = −3°, r = 0.93, 89 % of area within ±15°).